

UC-Net: Uncertainty Inspired RGB-D Saliency Detection via Conditional Variational Autoencoders

Jing Zhang^{1,4,5} Deng-Ping Fan^{2,6,*} Yuchao Dai³ Saeed Anwar^{1,5}

Fatemeh Sadat Saleh^{1,4} Tong Zhang¹ Nick Barnes¹

¹ Australian National University ² CS, Nankai University ³ Northwestern Polytechnical University

⁴ ACRV ⁵ Data61 ⁶ Inception Institute of Artificial Intelligence (IIAI), Abu Dhabi, UAE

Abstract

In this paper, we propose the first framework (UC-Net) to employ uncertainty for RGB-D saliency detection by learning from the data labeling process. Existing RGB-D saliency detection methods treat the saliency detection task as a point estimation problem, and produce a single saliency map following a deterministic learning pipeline. Inspired by the saliency data labeling process, we propose probabilistic RGB-D saliency detection network via conditional variational autoencoders to model human annotation uncertainty and generate multiple saliency maps for each input image by sampling in the latent space. With the proposed saliency consensus process, we are able to generate an accurate saliency map based on these multiple predictions. Quantitative and qualitative evaluations on six challenging benchmark datasets against 18 competing algorithms demonstrate the effectiveness of our approach in learning the distribution of saliency maps, leading to a new state-of-the-art in RGB-D saliency detection¹.

1. Introduction

Object-level visual saliency detection involves separating the most conspicuous objects that attract humans from the background [27, 2, 55, 63, 38, 29, 62]. Recently, visual saliency detection from RGB-D images have attracted lots of interest due to the importance of depth information in human vision system and the popularity of depth sensing technologies [61, 64]. Given a pair of RGB-D images, the task of RGB-D saliency detection aims to predict a saliency map by exploring the complementary information between color image and depth data.

The de-facto standard for RGB-D saliency detection is to train a deep neural network using ground truth (GT)

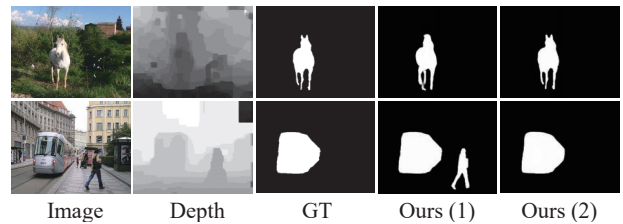


Figure 1. Provided GT compared with UC-Net (ours) predicted saliency maps. For images with a single salient object (1st row), we can produce consistent prediction. When multiple salient objects exist (2nd row), we can produce diverse predictions.

saliency maps provided by the corresponding benchmark datasets, where the GT saliency maps are obtained through human consensus or by the dataset creators [18]. Building upon large scale RGB-D datasets, deep convolutional neural network based models [21, 61, 6, 24] have made profound progress in learning the mapping from an RGB-D image pair to the corresponding GT saliency map. Considering the progress for RGB-D saliency detection under this pipeline, in this paper, we would like to argue that this pipeline fails to capture the *uncertainty* in labeling the GT saliency maps.

According to research in human visual perception [33], visual saliency detection is subjective to some extent. Each person could have specific preferences in labeling the saliency map (which has been previously discussed in user-specific saliency detection [26]). Existing approaches to RGB-D saliency detection treat saliency detection as a point estimation problem, and produce a single saliency map for each input image pair following a *deterministic* learning pipeline, which fails to capture the stochastic characteristic of saliency, and may lead to a partisan saliency model as shown in second row of Fig. 1. Instead of obtaining only a single saliency prediction (point estimation), we are interested in how the network produces multiple predictions (distribution estimation), which are then processed further to generate a single prediction in a similar way to how the GT saliency maps are created.

In this paper, inspired by human perceptual uncertainty,

*Corresponding author: Deng-Ping Fan (dengpfan@gmail.com)

¹Our code is publicly available at: <https://github.com/JingZhang617/UCNet>.

we propose a conditional variational autoencoders [50] (CVAE) based RGB-D saliency detection model *UC-Net* to produce multiple saliency predictions by modeling the distribution of output space as a generative model conditioned on the input RGB-D images to account for the human uncertainty in annotation.

However, there still exists one obstacle before we could apply the probabilistic framework, that is existing RGB-D benchmark datasets generally only provide a single GT saliency map for each RGB-D image pair. To produce diverse and accurate predictions², we resort to the “hide and seek” [49] principle following the orientation shifting theory [26] by iteratively hiding the salient foreground from the RGB image for testing, which forces the deep network to learn the saliency map with diversity. Through this iterative hiding strategy, we obtain multiple saliency maps for each input RGB-D image pair, which reflects the diversity/uncertainty from human labeling.

Moreover, depth data in the RGB-D saliency dataset can be noisy, and a direct fusion of RGB and depth information may overwhelm the network to fit noise. To deal with the noisy depth problem, a depth correction network is proposed as an auxiliary component to produce depth images with rich semantic and geometric information. We also introduce a saliency consensus module to mimic the majority voting mechanism for saliency GT generation.

Our main contributions are summarized as: 1) We propose a conditional probabilistic RGB-D saliency prediction model that can produce diverse saliency predictions instead of a single saliency map; 2) We provide a mechanism via saliency consensus to better model how saliency detection works; 3) We present a depth correction network to decrease noise that is inherent in depth data; 4) Extensive experimental results on six RGB-D saliency detection benchmark datasets demonstrate the effectiveness of our *UC-Net*.

2. Related Work

2.1. RGB-D Saliency Detection

Depend on how the complementary information between RGB images and depth images is fused, existing RGB-D saliency detection models can be roughly classified into three categories: early-fusion models [43], late-fusion models [54, 24] and cross-level fusion models [61, 5, 7, 6, 64]. Qu *et al.* [43] proposed an early-fusion model to generate feature for each superpixel of the RGB-D pair, which was then fed to a CNN to produce saliency of each superpixel. Recently, Wang *et al.* [54] introduced a late-fusion network (*i.e.* AFNet) to fuse predictions from the RGB and depth branch adaptively. In a similar pipeline, Han *et al.* [24]

fused the RGB and depth information through fully connected layers. Chen *et al.* [7] used a multi-scale multi-path network for different modality information fusion. Chen *et al.* [5] proposed a complementary-aware RGB-D saliency detection model by fusing features from the same stage of each modality with a complementary-aware fusion block. Chen *et al.* [6] presented attention-aware cross-level combination blocks for multi-modality fusion. Zhao *et al.* [64] integrated a contrast prior to enhance depth cues, and employed a fluid pyramid integration framework to achieve multi-scale cross-modal feature fusion. To effectively incorporate geometric and semantic information within a recurrent learning framework, Li *et al.* [61] introduced a depth-induced multi-scale RGB-D saliency detection network.

2.2. VAE or CVAE based Deep Probabilistic Models

Ever since the seminal work by Kingma *et al.* [31] and Rezende *et al.* [45], variational autoencoder (VAE) and its conditional counterpart CVAE [50] have been widely applied in various computer vision problems. To train a VAE, a reconstruction loss and a regularizer are needed to penalize the disagreement of the prior and posterior distribution of the latent representation. Instead of defining the prior distribution of the latent representation as a standard Gaussian distribution, CVAE utilizes the input observation to modulate the prior on Gaussian latent variables to generate the output. In low-level vision, VAE and CVAE have been applied to the tasks such as image background modeling [34], latent representations with sharp samples [25], difference of motion modes [57], medical image segmentation model [3], and modeling inherent ambiguities of an image [32]. Meanwhile, VAE and CVAE have been explored in more complex vision tasks such as uncertain future forecast [1, 53], human motion prediction [47], and shape-guided image generation [12]. Recently, VAE algorithms have been extended to 3D domain targeting applications such as 3D meshes deformation [52], and point cloud instance segmentation [59].

To the best of our knowledge, CVAE has not been exploited in saliency detection. Although Li *et al.* [34] adopted VAE in their saliency prediction framework, they used VAE to model the image background, and separated salient objects from the background through the reconstruction residuals. In contrast, we use CVAE to model labeling variants, indicating human uncertainty of labeling. We are the first to employ CVAE in saliency prediction network by considering the human uncertainty in annotation.

3. Our Model

In this section, we present our probabilistic RGB-D saliency detection model based on a conditional variational autoencoder, which learns the distribution of saliency maps rather than a single prediction. Let $\xi = \{X_i, Y_i\}_{i=1}^N$ be the training dataset, where $X_i = \{I_i, D_i\}$ denotes the RGB-D

²Diversity of prediction is related to the content of image. Image with clear content may lead to consistent prediction (1st row in Fig. 1), while complex image may produce diverse predictions (2nd row of Fig. 1).

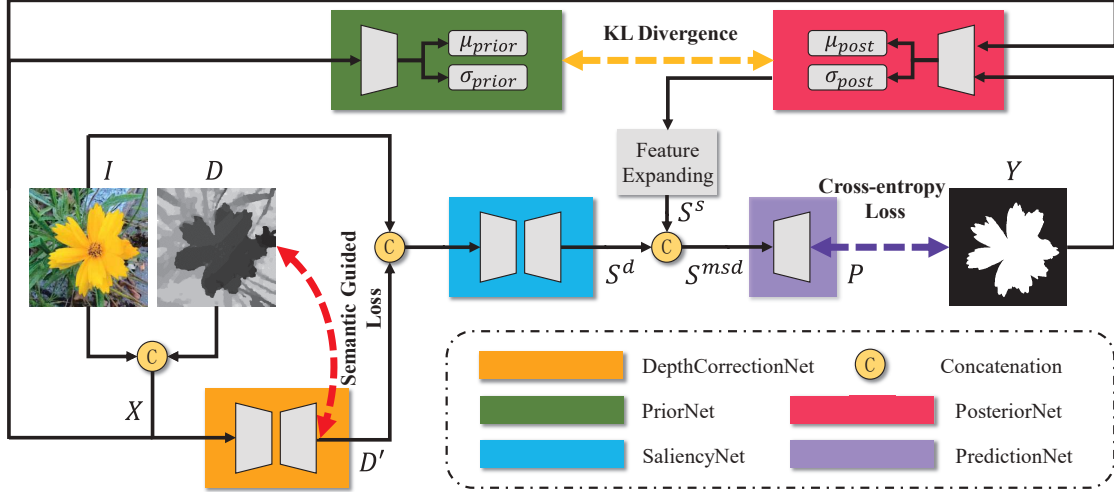


Figure 2. Network training pipeline. Four main modules are included, namely a LatentNet (PriorNet ($\mu_{\text{prior}}, \sigma_{\text{prior}}$) and PosteriorNet ($\mu_{\text{post}}, \sigma_{\text{post}}$)), a SaliencyNet, a DepthCorrectionNet and a PredictionNet. The LatentNet maps the RGB-D image pair X (or together with GT Y for the PosteriorNet) to low dimensional Gaussian latent variable z . The DepthCorrectionNet refines the raw depth with a semantic guided loss. The SaliencyNet takes the RGB image and the refined depth as input to generate a saliency feature map. The PredictionNet takes both stochastic features and deterministic features to produce a final saliency map. We perform saliency consensus in the testing stage, as shown in Fig. 3 to generate the final saliency map according to the mechanism of GT saliency map generation.



Figure 3. Overview of the proposed framework during testing. We sample the PriorNet multiple times to generate diverse and accurate predictions. The saliency consensus module is then used to obtain the majority voting of the final predictions.

input (consisting of the RGB image I_i and the depth image D_i), Y_i denotes the ground truth saliency map. The whole pipeline of our model during training and testing are illustrated in Fig. 2 and Fig. 3, respectively.

Our network is composed of five main modules: 1) LatentNet (PriorNet and PosteriorNet) that maps the RGB-D input X_i (for PriorNet) or X_i and Y_i (for PosteriorNet) to the low dimensional latent variables $z_i \in \mathbb{R}^K$ (K is dimension of the latent space); 2) DepthCorrectionNet that takes I_i and D_i as input to generate a refined depth image D'_i ; 3) SaliencyNet that maps the RGB image I_i and the refined depth image D'_i to saliency feature maps S^d_i ; 4) PredictionNet that employs stochastic features S^d_i from LatentNet and deterministic features S^msd_i from SaliencyNet to produce our saliency map prediction P_i ; 5) A saliency consensus module in the testing stage that mimics the mechanism of saliency GT generation to evaluate the performance with the provided single GT saliency map Y_i . We will introduce each module as follows.

3.1. Probabilistic RGB-D Saliency Model via CVAE

The Conditional Variational Autoencoder (CVAE) modulates the prior as a Gaussian distribution with parameters

conditioned on the input data X . There are three types of variables in the conditional generative model: conditioning variable X (RGB-D image pair in our setting), latent variable z , and output variable Y . For the latent variable z drawn from the Gaussian distribution $P_\theta(z|X)$, the output variable Y is generated from $P_\omega(Y|X, z)$, then the posterior of z is formulated as $Q_\phi(z|X, Y)$. The loss of CVAE is defined as:

$$\mathcal{L}_{\text{CVAE}} = E_{z \sim Q_\phi(z|X, Y)} [-\log P_\omega(Y|X, z)] + D_{KL}(Q_\phi(z|X, Y) || P_\theta(z|X)), \quad (1)$$

where $P_\omega(Y|X, z)$ is the likelihood of $P(Y)$ given latent variable z and conditioning variable X , the Kullback-Leibler Divergence $D_{KL}(Q_\phi(z|X, Y) || P_\theta(z|X))$ works as a regularization loss to reduce the gap between the prior $P_\theta(z|X)$ and the auxiliary posterior $Q_\phi(z|X, Y)$. In this way, CVAE aims to model the log likelihood $P(Y)$ under encoding error $D_{KL}(Q_\phi(z|X, Y) || P_\theta(z|X))$. Following the standard practice in conventional CVAE [50], we design a CVAE-based RGB-D saliency detection network, and describe each component of our model in the following.

LatentNet: We define $P_\theta(z|X)$ as PriorNet that maps the input RGB-D image pair X to a low-dimensional latent feature space, where θ is the parameter set of PriorNet. With the same network structure and provided GT saliency map Y , we define $Q_\phi(z|X, Y)$ as PosteriorNet, with ϕ being the posterior net parameter set. In the LatentNet (PriorNet and PosteriorNet), we use five convolutional layers to map the input RGB-D image X (or concatenation of X and Y for the PosteriorNet) to the latent Gaussian variable $z \sim \mathcal{N}(\mu, \text{diag}(\sigma^2))$, where $\mu, \sigma \in \mathbb{R}^K$, representing the



Figure 4. Detailed structure of LatentNet, where K is dimension of the latent space, “c1_4K” represents a 1×1 convolutional layer of output channel size $4K$, “GAP” is global average pooling.

mean and standard deviation of the latent Gaussian variable, as shown in Fig. 4.

Let us define parameter set of PriorNet and PosteriorNet as $(\mu_{\text{prior}}, \sigma_{\text{prior}})$ and $(\mu_{\text{post}}, \sigma_{\text{post}})$ respectively. The KL-Divergence in Eq. (1) is used to measure the distribution mismatch between the prior net $P_{\theta}(z|X)$ and posterior net $Q_{\phi}(z|X, Y)$, or how much information is lost when using $Q_{\phi}(z|X, Y)$ to represent $P_{\theta}(z|X)$. Typical using of CVAE involves multiple versions of ground truth Y [32] to produce informative $z \in \mathbb{R}^K$, with each position in z represents possible labeling variants or factors that may cause diverse saliency annotations. As we have only one version of GT, directly training with the provided single GT may fail to produce diverse predictions as the network will simply fit the provided annotation Y .

Generate Multiple Predictions: To produce diverse and accurate predictions, we propose an iterative hiding technique inspired by [49] following the orientation shifting theory [26] to generate more annotations as shown in Fig. 5. We iteratively hide the salient region in the RGB image with mean of the training dataset. The RGB image and its corresponding GT are set as the starting point of the “new label generation” technique. We first hide the ground truth salient object in the RGB image, and feed the modified image to an existing RGB saliency detection model [42] to produce a saliency map and treat it as one candidate annotation. We repeat salient object hiding technique three times for each training image³ to obtain four different sets of annotations in total (including the provided GT), and we term this dataset as “AugedGT”, which is our training dataset.

During training, different annotations (as shown in Fig. 5) in $Q_{\phi}(z|X, Y)$ can force the PriorNet $P_{\theta}(z|X)$ to encode labeling variants of a given input X . As we have already obtained diverse annotations with the proposed hiding technique, we are expecting the network to produce diverse predictions for images with complicated context. During testing, we can obtain one stochastic feature S^s (input of the “PredictionNet”) of channel size K each time we sample as shown in Fig. 3.

SaliencyNet: We design SaliencyNet to produce a deterministic saliency feature map S^d from the input RGB-D data, where the refined depth data comes from the Depth-CorrectionNet. We use VGG16 [48] as our encoder, and remove layers after the fifth pooling layer. To enlarge the receptive field, we follow DenseASPP [58] to obtain feature

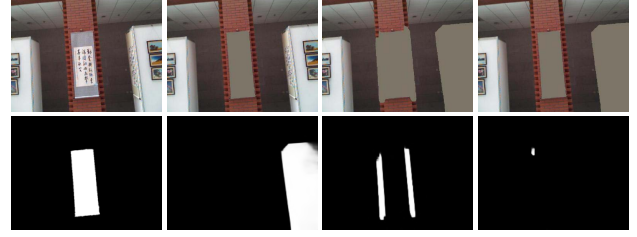


Figure 5. New label generation. The 1st row: we iteratively hide the predicted salient region, where no region is hidden in the first image. The 2nd row: the corresponding GT of the hidden image.

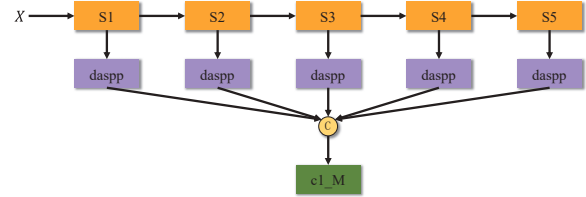


Figure 6. SaliencyNet, where “S1” represents the first stage of the VGG16 network, “daspp” is the DenseASPP module [58].

map with the receptive field of the whole image on each stage of the VGG16 network. We then concatenate those feature maps and feed it to another convolutional layer to obtain S^d . The detail of the SaliencyNet is illustrated in Fig. 6, where “c1_M” represents convolutional layer of kernel size 1×1 , and M is channel size of S^d .

Feature Expanding: Statistics ($z \sim \mathcal{N}(\mu, \text{diag}(\sigma^2))$ in particular) from the LatentNet (PriorNet during testing as shown in Fig. 3 “Sampling”, or PosteriorNet during training in Fig. 2) form the input to the Feature Expanding module. Given a pair of (μ^k, σ^k) in each position of the K dimensional vector, we obtain latent vector $z^k = \sigma^k \odot \epsilon + \mu^k$, where $\epsilon \in \mathcal{N}(0, \mathbf{I})$. To fuse with deterministic feature S^d , we expand z^k to feature map of the same spatial size as S^d by defining ϵ as two-dimensional Gaussian noise map. With $k = 1, \dots, K$, we can obtain a K (size of the latent space) channel stochastic feature S^s representing labeling variants.

PredictionNet: The LatentNet produces stochastic features S^s representing labeling variants, while the SaliencyNet outputs deterministic saliency features S^d of input X . We propose the PredictionNet, as shown in Fig. 2 to fuse features from mentioned branches. A naive concatenation of S^s and S^d may lead the network to learn only from the deterministic features, thus fail to model labeling variants. Inspired by [47], we mix S^s and S^d channel-wisely; thus, the network cannot distinguish between features of the deterministic branch and the probabilistic branch. We concatenate S^d and S^s to form a $K + M$ channel feature map S^{sd} . We define $K + M$ dimensional variable r (a learnable parameter) representing possible ranking of $1, 2, \dots, K + M$, and then S^{sd} is mixed channel-wisely according to r to obtain the mixed feature S^{msd} . Three 1×1 convolutional layers with output channel sizes of $K, K/2, 1$, are included in

³We found that usually after three times of hiding, there exists no salient objects in the hidden image.

the PredictionNet to map S^{msd} to a single channel saliency map P . During testing, with multiple stochastic features S^s , we can obtain multiple predictions by sampling S^s from the LatentNet $\mathcal{N}(\mu_{\text{prior}}, \text{diag}(\sigma_{\text{prior}}^2))$ multiple times.

3.2. DepthCorrectionNet

Two main approaches are employed to acquire depth data for RGB-D saliency detection: through depth sensors such as Microsoft Kinect, *e.g.*, DES [8], and NLPR [41] datasets; or computing depth from stereo cameras, examples of such datasets are SSB [40] and NJU2K [28]. Regardless of the capturing technique, noise is inherent in the depth data. We propose a semantic guided depth correction network to produce refined depth information as shown in Fig. 2, termed as “DepthCorrectionNet”. The encoder part of the DepthCorrectionNet is the same as the “SaliencyNet”, while the decoder part is composed of four sequential convolutional layers and bilinear upsampling operation.

We assume that edges of the depth map should be aligned with edges of the RGB image. We adopt the boundary IOU loss [39] as a regularizer for DepthCorrectionNet to achieve a refined depth, which is guided by intensity of the RGB image. The full loss for DepthCorrectionNet is defined as:

$$\mathcal{L}_{\text{Depth}} = \mathcal{L}_{sl} + \mathcal{L}_{\text{IouB}}, \quad (2)$$

where \mathcal{L}_{sl} is the smooth ℓ_1 loss between the refined depth D' and the raw depth D , $\mathcal{L}_{\text{IouB}}$ is the boundary IOU loss between the refined depth D' and intensity I_g of the RGB image I . Given the predicted depth map D' and intensity of RGB image I_g , we follow [39] to compute the first-order derivatives of D' and I_g . Subsequently, we calculate the magnitude gD' and gI of the gradients of D' and I_g , and define the boundary IOU loss as:

$$\mathcal{L}_{\text{IouB}} = 1 - 2 \frac{|gD' \cap gI|}{|gD'| + |gI|}. \quad (3)$$

3.3. Saliency Consensus Module

Saliency detection is subjective to some extent, and it is common to have multiple annotators to label one image, and the final ground truth saliency map is obtained through majority voting strategy [18]. Although it is well known in the saliency detection community about how the ground truth is acquired; yet, there exists no research on embedding this mechanism into deep saliency frameworks. *Current models define saliency detection as a point estimation problem instead of a distribution estimation problem.* We, instead, use CVAE to obtain the saliency distribution. Next, we embed saliency consensus into our probabilistic framework to compute the majority voting of different predictions in the testing stage as shown in Fig. 3.

During testing, we sample PriorNet with fixed μ_{prior} and σ_{prior} to obtain a stochastic feature S^s . With each S^s and deterministic feature S^d from SaliencyNet, we obtain one

version of saliency prediction P . To obtain C different predictions P^1, \dots, P^C , we sample PriorNet C times. We simultaneously feed these multiple predictions to the saliency consensus module to obtain the consensus of predictions.

Given multiple predictions $\{P^c\}_{c=1}^C$, where $P^c \in [0, 1]$, we first compute the binary⁴ version P_b^c of the predictions by performing adaptive threshold [4] on P^c . For each pixel (u, v) , we obtain a C dimensional feature vector $P_{u,v} \in \{0, 1\}^C$. We define $P_b^{mjv} \in \{0, 1\}$ as a one-channel saliency map representing majority voting of $P_{u,v}$. We define an indicator $1^c(u, v) = \mathbf{1}(P_b^c(u, v) = P_b^{mjv}(u, v))$ representing whether the binary prediction is consistent with the majority voting of the predictions. If $P_b^c(u, v) = P_b^{mjv}(u, v)$, then $1^c(u, v) = 1$. Otherwise, $1^c(u, v) = 0$. We obtain one gray saliency map after saliency consensus as:

$$P_g^{mjv}(u, v) = \frac{\sum_{c=1}^C 1^c(u, v)}{C} \sum_{c=1}^C (P_b^c(u, v) \times 1^c(u, v)). \quad (4)$$

3.4. Objective Function

At this stage, our loss function is composed of two parts *i.e.* $\mathcal{L}_{\text{CVAE}}$ and $\mathcal{L}_{\text{Depth}}$. Furthermore, we propose to use the smoothness loss [9] as a regularizer to achieve edge-aware saliency detection, based on the assumption of inter-class distinction and intra-class similarity. Following [56], we define first-order derivatives of the saliency map in the smoothness term as

$$\mathcal{L}_{\text{Smooth}} = \sum_{u,v} \sum_{d \in \vec{x}, \vec{y}} \Psi(|\partial_d P_{u,v}| e^{-\alpha |\partial_d I_g(u,v)|}), \quad (5)$$

where Ψ is defined as $\Psi(s) = \sqrt{s^2 + 1}e^{-6}$, $P_{u,v}$ is the predicted saliency map at position (u, v) , and $I_g(u, v)$ is the image intensity, d indexes over partial derivative on \vec{x} and \vec{y} directions. We set $\alpha = 10$ following [56].

Both the smoothness loss (Eq. (5)) and the boundary IOU loss (Eq. (3)) need intensity I_g . We convert the RGB image I to a gray-scale intensity image I_g as [60]:

$$I_g = 0.2126 \times I^{lr} + 0.7152 \times I^{lg} + 0.0722 \times I^{lb}, \quad (6)$$

where I^{lr} , I^{lg} and I^{lb} represent the color components in the linear color space after Gamma function been removed from the original color space. I^{lr} is achieved via:

$$I^{lr} = \begin{cases} \frac{I^r}{12.92}, & I^r \leq 0.04045, \\ \left(\frac{I^r + 0.055}{1.055} \right)^{2.4}, & I^r > 0.04045. \end{cases} \quad (7)$$

where I^r is the original red channel of image I , and we compute I^g and I^b in the same way as Eq. (7).

⁴As the GT map $Y \in \{0, 1\}$, we produce series of binary predictions with each one representing annotation from one saliency annotator.

With smoothness loss $\mathcal{L}_{\text{Smooth}}$, depth loss $\mathcal{L}_{\text{Depth}}$ and CVAE loss $\mathcal{L}_{\text{CVAE}}$, our final loss function is defined as:

$$\mathcal{L}_{\text{sal}} = \mathcal{L}_{\text{CVAE}} + \lambda_1 \mathcal{L}_{\text{Depth}} + \lambda_2 \mathcal{L}_{\text{Smooth}}. \quad (8)$$

In our experiments, we set $\lambda_1 = \lambda_2 = 0.3$.

Training details: We set channel size of S^d as $M = 32$, and scale of latent space as $K = 8$. We trained our model using Pytorch, and initialized the encoder of SaliencyNet and DepthCorrectionNet with VGG16 parameters pre-trained on ImageNet. Weights of new layers were initialized with $\mathcal{N}(0, 0.01)$, and bias was set as constant. We used the Adam method with momentum 0.9 and decreased the learning rate 10% after each epoch. The base learning rate was initialized as $1e-4$. The whole training took 13 hours with training batch size 6 and maximum epoch 30 on a PC with an NVIDIA GeForce RTX GPU. For input image size 352×352 , the inference time is 0.06s on average.

4. Experimental Results

4.1. Setup

Datasets: We perform experiments on six datasets including five widely used RGB-D saliency detection datasets (namely NJU2K [28], NLPR [41], SSB [40], LFSD [35], DES [8]) and one newly released dataset (SIP [18]).

Competing Methods: We compare our method with 18 algorithms, including ten handcrafted conventional methods and eight deep RGB-D saliency detection models.

Evaluation Metrics: Four evaluation metrics are used, including two widely used: 1) Mean Absolute Error (MAE \mathcal{M}); 2) mean F-measure (F_β) and two recently proposed: 3) Enhanced alignment measure (mean E-measure, E_ϵ) [15] and 4) Structure measure (S-measure, S_α) [14].

4.2. Performance Comparison

Quantitative Comparison: We report performance of our method and competing methods in Table 1. It shows that our method consistently achieves the best performance on all datasets, especially on SSB [40] and SIP [18], our method achieves significant S-measure, E-measure, and F-measure performance boost and a decrease in MAE by a large margin. We show E-measure and F-measure curves of competing methods and ours in Fig. 7. We observe that our method produces not only stable E-measure and F-measure but also best performance.

Qualitative Comparisons: In Fig. 8, we show five images comparing results of our method with one newly released RGB-D saliency detection method (DMRA [61]), and two widely used methods to produce structured outputs, namely M-head [46] and MC-dropout [30] (we will discuss these two methods in detail in the ablation study section). We design both M-head and MC-dropout based structured saliency detection models by replacing CVAE with M-head

and MC-dropout respectively. Results in Fig. 8 show that our method can not only produce high accuracy predictions (compared with DMRA [61]), but also diverse predictions (compared with M-head based and MC-dropout based models) for images with complex background (image in the first and last rows).

4.3. Ablation Study

We carried out eight experiments (shown in Table 2) to thoroughly analyse our framework, including network structure (“M1”, “M2”, “M3”), probabilistic model selection (“M4”, “M5”, “M6”), data source selection (“M7”) and effectiveness of the new label generation technique (“M8”). We make the number bold when it’s better than ours.

Scale of Latent Space: We investigate the influence of the scale of the Gaussian latent space K in our network. In this paper, after parameter tuning, we find $K = 8$ works best. We show performance with $K = 32$ as “M1”. Performance of “M1” is worse than our reported results, which indicates that scale of the latent space is an important parameter in our framework. We further carried out more experiments with $K \in [2, 12]$, and found relative stable predictions with $K \in [6, 10]$.

Effect of DepthCorrectionNet: To illustrate the effectiveness of the proposed DepthCorrectionNet, we remove this branch and feed the concatenation of the RGB image and depth data to the SaliencyNet, shown as “M2”, which is worse than our method. On DES [8] dataset, we observe the proposed solution achieves around 4% improvement on S-measure, E-measure and F-measure, which demonstrates the effectiveness of the depth correction net.

Saliency Consensus Module: To mimic the saliency labeling process, we embed a saliency consensus module during test in our framework (as shown in Fig. 3) to obtain the majority voting of the multiple predictions. We remove it from our framework and test the network performance by random sample from the latent PriorNet $P_\theta(z|X)$, and performance is shown in “M3”, which is the best compared with competing methods. While, with the saliency consensus module embedded, we achieve even better performance, which illustrates effectiveness of the saliency consensus module.

VAE vs. CVAE: We use CVAE to model labeling variants, and a PosteriorNet is used to estimate parameters for the PriorNet. To test how our model performs with prior of z as a standard normal distribution, and the posterior of z as $P_\theta(z|X)$. VAE performance is shown as “M4”, which is comparable with SOTA RGB-D models. With the CVAE [50] based model proposed, we further boost performance of “M4”, which proves effectiveness of the our solution.

Multi-head vs. CVAE: Multi-head models [46] generate multiple predictions with different decoders and a shared encoder, and the loss function is always defined as the closest of the multiple predictions. We remove the LatentNet,

Table 1. Benchmarking results of ten leading handcrafted feature-based models and eight deep models on six RGBD saliency datasets. \uparrow & \downarrow denote larger and smaller is better, respectively. Here, we adopt mean F_β and mean E_ξ [15].

	Metric	Handcrafted Feature based Models										Deep Models								UC-Net Ours
		LHM [41]	CDB [36]	DESM [8]	GP [44]	CDCP [66]	ACSD [28]	LBE [20]	DCMC [10]	MDSF [51]	SE [22]	DF [43]	AFNet [54]	CTMF [24]	MMCI [7]	PCF [5]	TANet [6]	CPFP [64]	DMRA [61]	
NJU2K [28]	$S_\alpha \uparrow$.514	.632	.665	.527	.669	.699	.695	.686	.748	.664	.763	.822	.849	.858	.877	.879	.878	.886	.897
	$F_\beta \uparrow$.328	.498	.550	.357	.595	.512	.606	.556	.628	.583	.653	.827	.779	.793	.840	.841	.850	.873	.886
	$E_\xi \uparrow$.447	.572	.590	.466	.706	.594	.655	.619	.677	.624	.700	.867	.846	.851	.895	.895	.910	.920	.930
	$\mathcal{M} \downarrow$.205	.199	.283	.211	.180	.202	.153	.172	.157	.169	.140	.077	.085	.079	.059	.061	.053	.051	.043
SSB [40]	$S_\alpha \uparrow$.562	.615	.642	.588	.713	.692	.660	.731	.728	.708	.757	.825	.848	.873	.875	.871	.879	.835	.903
	$F_\beta \uparrow$.378	.489	.519	.405	.638	.478	.501	.590	.527	.611	.617	.806	.758	.813	.818	.828	.841	.837	.884
	$E_\xi \uparrow$.484	.561	.579	.508	.751	.592	.601	.655	.614	.664	.692	.872	.841	.873	.887	.893	.911	.879	.938
	$\mathcal{M} \downarrow$.172	.166	.295	.182	.149	.200	.250	.148	.176	.143	.141	.075	.086	.068	.064	.060	.051	.066	.039
DES [8]	$S_\alpha \uparrow$.578	.645	.622	.636	.709	.728	.703	.707	.741	.741	.752	.770	.863	.848	.842	.858	.872	.900	.934
	$F_\beta \uparrow$.345	.502	.483	.412	.585	.513	.576	.542	.523	.618	.604	.713	.756	.735	.765	.790	.824	.873	.919
	$E_\xi \uparrow$.477	.562	.566	.503	.748	.613	.650	.631	.621	.706	.684	.809	.826	.825	.838	.863	.888	.933	.967
	$\mathcal{M} \downarrow$.114	.100	.299	.168	.115	.169	.208	.111	.122	.090	.093	.068	.055	.065	.049	.046	.038	.030	.019
NLPR [41]	$S_\alpha \uparrow$.630	.632	.572	.655	.727	.673	.762	.724	.805	.756	.806	.799	.860	.856	.874	.886	.888	.899	.920
	$F_\beta \uparrow$.427	.421	.430	.451	.609	.429	.636	.542	.649	.624	.664	.755	.740	.737	.802	.819	.840	.865	.891
	$E_\xi \uparrow$.560	.567	.542	.571	.782	.579	.719	.684	.745	.742	.757	.851	.840	.841	.887	.902	.918	.940	.951
	$\mathcal{M} \downarrow$.108	.108	.312	.146	.112	.179	.081	.117	.095	.091	.079	.058	.056	.059	.044	.041	.036	.031	.025
LFSD [35]	$S_\alpha \uparrow$.557	.520	.722	.640	.717	.734	.736	.753	.700	.698	.791	.738	.796	.787	.794	.801	.828	.847	.864
	$F_\beta \uparrow$.396	.376	.612	.519	.680	.566	.612	.655	.521	.640	.679	.736	.756	.722	.761	.771	.811	.845	.855
	$E_\xi \uparrow$.491	.465	.638	.584	.754	.625	.670	.682	.588	.653	.725	.796	.810	.775	.818	.821	.863	.893	.901
	$\mathcal{M} \downarrow$.211	.218	.248	.183	.167	.188	.208	.155	.190	.167	.138	.134	.119	.132	.112	.111	.088	.075	.066
SIP [18]	$S_\alpha \uparrow$.511	.557	.616	.588	.595	.732	.727	.683	.717	.628	.653	.720	.716	.833	.842	.835	.850	.806	.875
	$F_\beta \uparrow$.287	.341	.496	.411	.482	.542	.572	.500	.568	.515	.465	.702	.608	.771	.814	.803	.821	.811	.867
	$E_\xi \uparrow$.437	.455	.564	.511	.683	.614	.651	.598	.645	.592	.565	.793	.704	.845	.878	.870	.893	.844	.914
	$\mathcal{M} \downarrow$.184	.192	.298	.173	.224	.172	.200	.186	.167	.164	.185	.118	.139	.086	.071	.075	.064	.085	.051

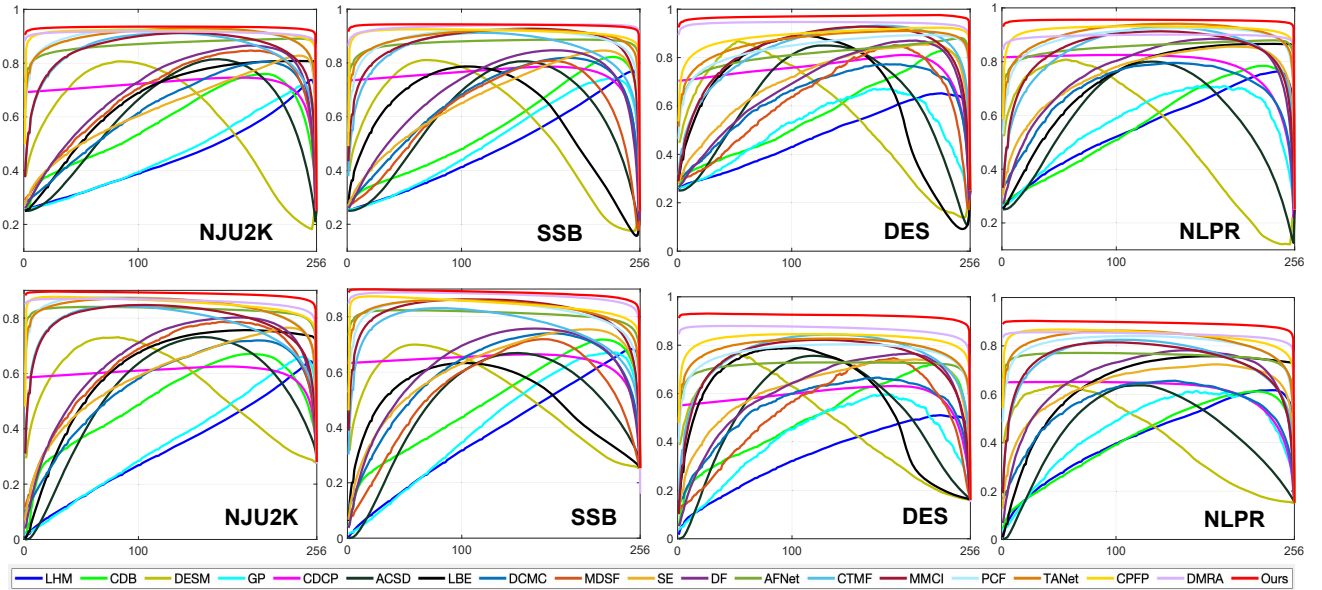


Figure 7. E-measure (1st row) and F-measure (2nd row) curves on four testing datasets.

and copy the decoder of the SaliencyNet multiple times to achieve multiple predictions (“M5” in this paper). We report performance in “M5” as mean of the multiple predictions. “M5” is better than SOTA models (e.g., DMRA) while there still exists gap between M-head based method (“M5”) and our CVAE based model (UC-Net).

Monte-Carlo Dropout vs. CVAE: Monte-Carlo Dropout [30] uses dropout during the testing stage to introduce stochastic to the network. We follow [30] to remove the LatentNet, and use dropout in the encoder and decoder of the

SaliencyNet in the testing stage. We repeats five times of random dropout (dropout ratio = 0.1), and report the mean performance as “M6”. Similar to “M5”, “M6” also achieves the best performance comparing with SOTA models (e.g., CPFP and DMRA), while the proposed CVAE based model achieves even better performance.

HHA vs. Depth: HHA [23] is a widely used technique that encodes the depth data to three channels: **h**orizontal disparity, **h**eight above ground, and the **a**ngle the pixels local surface normal makes with the inferred gravity direction.

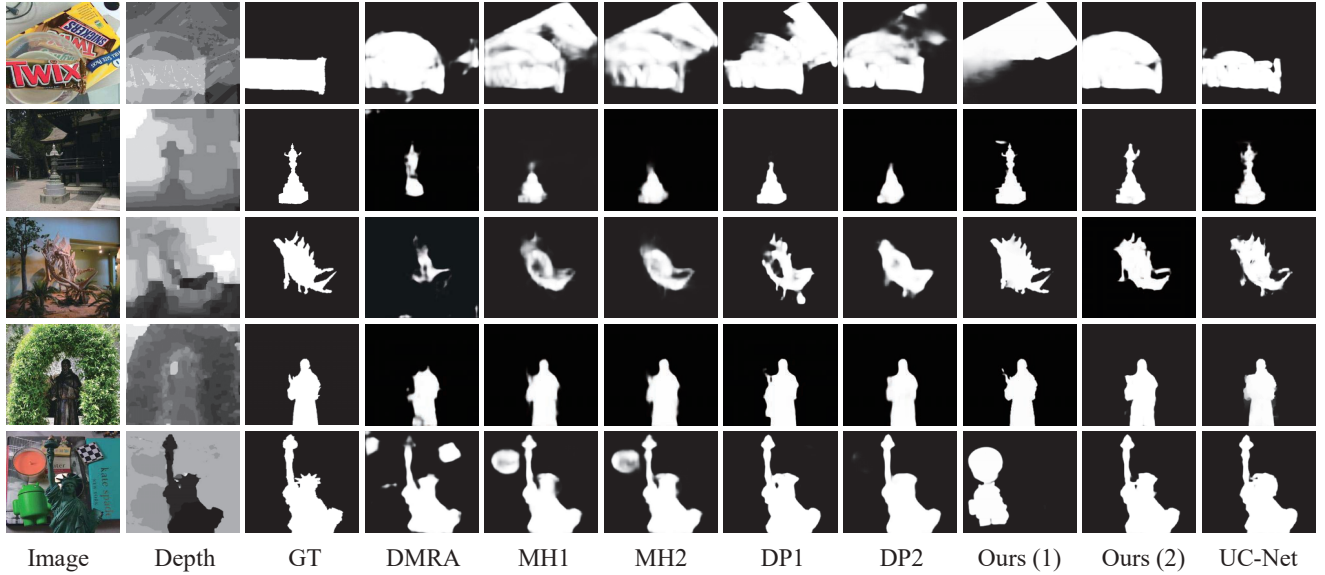


Figure 8. Comparisons of saliency maps. “MH1” and “MH2” are two predictions from M-head. “DP1” and “DP2” are predictions of two random MC-dropout during test. “Ours(1)” and “Ours(2)” are two predictions sampled from our CVAE based model. Different from M-head and MC-dropout, which produce consistent predictions for ambiguous images (5th row), *UC-Net* can produce diverse predictions.

Table 2. Ablation study on RGB-D saliency datasets.

	Metric	<i>UC-Net</i>	M1	M2	M3	M4	M5	M6	M7	M8	M9
<i>NJUZK</i> [28]	$S_\alpha \uparrow$.897	.866	.893	.905	.871	.885	.881	.893	.838	.866
	$F_\beta \uparrow$.886	.858	.887	.884	.851	.878	.878	.884	.787	.812
	$E_\xi \uparrow$.930	.905	.930	.927	.910	.923	.927	.932	.840	.866
	$\mathcal{M} \downarrow$.043	.060	.046	.045	.059	.047	.046	.044	.084	.075
<i>SSB</i> [40]	$S_\alpha \uparrow$.903	.854	.893	.900	.867	.891	.893	.898	.855	.872
	$F_\beta \uparrow$.884	.831	.876	.868	.834	.864	.876	.882	.793	.805
	$E_\xi \uparrow$.938	.894	.911	.922	.907	.921	.931	.934	.854	.870
	$\mathcal{M} \downarrow$.039	.060	.043	.047	.057	.047	.043	.040	.073	.068
<i>DES</i> [8]	$S_\alpha \uparrow$.934	.876	.896	.928	.897	.911	.896	.918	.811	.911
	$F_\beta \uparrow$.919	.844	.868	.902	.867	.897	.868	.904	.724	.843
	$E_\xi \uparrow$.967	.906	.928	.947	.930	.945	.928	.953	.794	.910
	$\mathcal{M} \downarrow$.019	.035	.026	.024	.033	.024	.026	.023	.065	.036
<i>NLPR</i> [41]	$S_\alpha \uparrow$.920	.878	.919	.918	.890	.899	.910	.915	.850	.883
	$F_\beta \uparrow$.891	.846	.897	.878	.845	.875	.867	.889	.759	.795
	$E_\xi \uparrow$.951	.911	.953	.941	.924	.937	.933	.951	.841	.883
	$\mathcal{M} \downarrow$.025	.039	.024	.029	.037	.029	.028	.025	.057	.045
<i>LFSD</i> [35]	$S_\alpha \uparrow$.864	.799	.847	.862	.820	.838	.847	.853	.729	.823
	$F_\beta \uparrow$.855	.791	.838	.841	.802	.833	.838	.848	.661	.779
	$E_\xi \uparrow$.901	.829	.879	.885	.865	.875	.879	.891	.720	.818
	$\mathcal{M} \downarrow$.066	.101	.079	.075	.093	.079	.079	.073	.145	.108
<i>SIP</i> [18]	$S_\alpha \uparrow$.875	.846	.867	.870	.851	.859	.867	.865	.810	.845
	$F_\beta \uparrow$.867	.837	.860	.848	.821	.853	.860	.855	.751	.795
	$E_\xi \uparrow$.914	.884	.908	.901	.893	.905	.908	.908	.816	.852
	$\mathcal{M} \downarrow$.051	.068	.056	.059	.067	.057	.056	.056	.094	.079

HHA is widely used in RGB-D related dense prediction models [11, 24] to obtain better feature representation. To test if HHA also works in our scenario, we replace depth with HHA, and performance is shown in “M7”. We observe similar performance achieved with HHA instead of the raw depth data.

New Label Generation: To produce diverse predictions, we follow [49] and generate diverse annotations for the training dataset. To illustrate the effectiveness of this strategy, we train with only the SaliencyNet to produce single channel saliency map with RGB-D image as input for simplicity. “M8” and “M9” represent using the provided train-

ing dataset and augmented training data respectively. We observe performance improvement of “M9” compared with “M8”, which indicates effectiveness of the new label generation technique.

5. Conclusion

Inspired by human uncertainty in ground truth (GT) annotation, we proposed the first uncertainty network named *UC-Net* for RGB-D saliency detection based on a conditional variational autoencoder. Different from existing methods, which generally treat saliency detection as a point estimation problem, we propose to learn the distribution of saliency maps. Under our formulation, our model is able to generate multiple labels which have been discarded in the GT annotation generation process through saliency consensus. Quantitative and qualitative evaluations on six standard and challenging benchmark datasets demonstrated the superiority of our approach in learning the distribution of saliency maps. In the future, we would like to extend our approach to other saliency detection problems (*e.g.*, VSOD [19], RGB SOD [13, 65], Co-SOD [17]). Furthermore, we plan to capture new datasets with multiple human annotations to further model the statistics of human uncertainty in interactive image segmentation [37], camouflaged object detection [16], *etc.*

Acknowledgments. This research was supported in part by Natural Science Foundation of China grants (61871325, 61420106007, 61671387), the Australia Research Council Centre of Excellence for Robotics Vision (CE140100016), and the National Key Research and Development Program of China under Grant 2018AAA0102803. We thank all reviewers and Area Chairs for their constructive comments.

References

- [1] Abubakar Abid and James Y. Zou. Contrastive Variational Autoencoder Enhances Salient Features. *CoRR*, abs/1902.04601, 2019.
- [2] Radhakrishna Achanta, Sheila Hemami, Francisco Estrada, and Sabine Susstrunk. Frequency-tuned salient region detection. In *IEEE CVPR*, pages 1597–1604, 2009.
- [3] Christian F. Baumgartner, Kerem Can Tezcan, Krishna Chaitanya, Andreas M. Hötker, Urs J. Muehlemaier, Khoshy Schawkat, Anton S. Becker, Olivio Donati, and Ender Konukoglu. PHiSeg: Capturing Uncertainty in Medical Image Segmentation. In *MICCAI*, pages 119–127, 2019.
- [4] Ali Borji, Ming-Ming Cheng, Huaizu Jiang, and Jia Li. Salient Object Detection: A Benchmark. *IEEE TIP*, 24(12):5706–5722, 2015.
- [5] Hao Chen and Youfu Li. Progressively complementarity-aware fusion network for RGB-D Salient Object Detection. In *IEEE CVPR*, pages 3051–3060, 2018.
- [6] Hao Chen and Youfu Li. Three-stream Attention-aware Network for RGB-D Salient Object Detection. *IEEE TIP*, pages 2825–2835, 2019.
- [7] Hao Chen, Youfu Li, and Dan Su. Multi-modal fusion network with multi-scale multi-path and cross-modal interactions for RGB-D salient object detection. *PR*, 86:376–385, 2019.
- [8] Yupeng Cheng, Huazhu Fu, Xingxing Wei, Jiangjian Xiao, and Xiaochun Cao. Depth enhanced saliency detection method. In *ACM ICIMCS*, pages 23–27, 2014.
- [9] Gabriel J. Brostow Clement Godard, Oisín Mac Aodha. Unsupervised Monocular Depth Estimation with Left-Right Consistency. In *IEEE CVPR*, pages 6602–6611, 2017.
- [10] Runmin Cong, Jianjun Lei, Changqing Zhang, Qingming Huang, Xiaochun Cao, and Chunping Hou. Saliency detection for stereoscopic images based on depth confidence analysis and multiple cues fusion. *IEEE SPL*, 23(6):819–823, 2016.
- [11] Dapeng Du, Limin Wang, Huiling Wang, Kai Zhao, and Gangshan Wu. Translate-to-Recognize Networks for RGB-D Scene Recognition. In *IEEE CVPR*, pages 11836–11845, 2019.
- [12] Patrick Esser, Ekaterina Sutter, and Björn Ommer. A Variational U-Net for Conditional Appearance and Shape Generation. In *IEEE CVPR*, pages 8857–8865, 2018.
- [13] Deng-Ping Fan, Ming-Ming Cheng, Jiang-Jiang Liu, Shang-Hua Gao, Qibin Hou, and Ali Borji. Salient objects in clutter: Bringing salient object detection to the foreground. In *ECCV*, pages 186–202, 2018.
- [14] Deng-Ping Fan, Ming-Ming Cheng, Yun Liu, Tao Li, and Ali Borji. Structure-measure: A new way to evaluate foreground maps. In *IEEE ICCV*, pages 4548–4557, 2017.
- [15] Deng-Ping Fan, Cheng Gong, Yang Cao, Bo Ren, Ming-Ming Cheng, and Ali Borji. Enhanced-alignment Measure for Binary Foreground Map Evaluation. In *IJCAI*, pages 698–704, 2018.
- [16] Deng-Ping Fan, Ge-Peng Ji, Guolei Sun, Ming-Ming Cheng, Jianbing Shen, and Ling Shao. Camouflaged Object Detection. In *IEEE CVPR*, 2020.
- [17] Deng-Ping Fan, Zheng Lin, Ge-Peng Ji, Dingwen Zhang, Huazhu Fu, and Ming-Ming Cheng. Taking a Deeper Look at the Co-salient Object Detection. In *IEEE CVPR*, 2020.
- [18] Deng-Ping Fan, Zheng Lin, Zhao Zhang, Menglong Zhu, and Ming-Ming Cheng. Rethinking RGB-D salient object detection: Models, datasets, and large-scale benchmarks. *IEEE TNNLS*, 2020.
- [19] Deng-Ping Fan, Wenguan Wang, Ming-Ming Cheng, and Jianbing Shen. Shifting more attention to video salient object detection. In *IEEE CVPR*, pages 8554–8564, 2019.
- [20] David Feng, Nick Barnes, Shaodi You, and Chris McCarthy. Local background enclosure for RGB-D salient object detection. In *IEEE CVPR*, pages 2343–2350, 2016.
- [21] Keren Fu, Deng-Ping Fan, Ge-Peng Ji, and Qijun Zhao. JL-DCF: Joint Learning and Densely-Cooperative Fusion Framework for RGB-D Salient Object Detection. In *IEEE CVPR*, 2020.
- [22] Jingfan Guo, Tongwei Ren, and Jia Bei. Salient object detection for rgb-d image via saliency evolution. In *ICME*, pages 1–6, 2016.
- [23] Saurabh Gupta, Ross Girshick, Pablo Arbeláez, and Jitendra Malik. Learning rich features from RGB-D images for object detection and segmentation. In *ECCV*, pages 345–360, 2014.
- [24] Junwei Han, Hao Chen, Nian Liu, Chenggang Yan, and Xuelong Li. CNNs-based RGB-D saliency detection via cross-view transfer and multiview fusion. *IEEE TCYB*, pages 3171–3183, 2018.
- [25] Faruk Ahmed Adrien Ali Taga Francesco Visin David Vázquez Aaron C. Courville Ishaan Gulrajani, Kundan Kumar. PixelVAE: A Latent Variable Model for Natural Images. In *ICLR*, 2016.
- [26] Laurent Itti and Christof Koch. A saliency-based search mechanism for overt and covert shifts of visual attention. *VR*, 40(10):1489 – 1506, 2000.
- [27] Laurent Itti, Christof Koch, and Ernst Niebur. A model of saliency-based visual attention for rapid scene analysis. *IEEE TPAMI*, 20(11):1254–1259, 1998.
- [28] Ran Ju, Ling Ge, Wenjing Geng, Tongwei Ren, and Gangshan Wu. Depth saliency based on anisotropic center-surround difference. In *ICIP*, pages 1115–1119, 2014.
- [29] Shuhui Wang Jun Wei and Qingming Huang. F3Net: Fusion, Feedback and Focus for Salient Object Detection. In *AAAI*, 2020.
- [30] Alex Kendall, Vijay Badrinarayanan, , and Roberto Cipolla. Bayesian SegNet: Model Uncertainty in Deep Convolutional Encoder-Decoder Architectures for Scene Understanding. In *BMVC*, 2017.
- [31] Diederik P Kingma and Max Welling. Auto-Encoding Variational Bayes. In *ICLR*, 2013.
- [32] Simon Kohl, Bernardino Romera-Paredes, Clemens Meyer, Jeffrey De Fauw, Joseph R. Ledsam, Klaus Maier-Hein, S. M. Ali Eslami, Danilo Jimenez Rezende, and Olaf Ronneberger. A Probabilistic U-Net for Segmentation of Ambiguous Images. In *NeurIPS*, pages 6965–6975, 2018.
- [33] Olivier Le Meur and Thierry Baccino. Methods for comparing scanpaths and saliency maps: strengths and weaknesses. *Behavior Research Methods*, 45(1):251–266, 2013.

- [34] Bo Li, Zhengxing Sun, and Yuqi Guo. SuperVAE: Superpixelwise Variational Autoencoder for Salient Object Detection. In *AAAI*, pages 8569–8576, 2019.
- [35] Nianyi Li, Jinwei Ye, Yu Ji, Haibin Ling, and Jingyi Yu. Saliency detection on light field. In *IEEE CVPR*, pages 2806–2813, 2014.
- [36] Fangfang Liang, Lijuan Duan, Wei Ma, Yuanhua Qiao, Zhi Cai, and Laiyun Qing. Stereoscopic saliency model using contrast and depth-guided-background prior. *Neurocomputing*, 275:2227–2238, 2018.
- [37] Zheng Lin, Zhao Zhang, Lin-Zhuo Chen, Ming-Ming Cheng, and Shao-Ping Lu. Interactive Image Segmentation with First Click Attention. In *IEEE CVPR*, 2020.
- [38] Yi Liu, Qiang Zhang, Dingwen Zhang, and Jungong Han. Employing Deep Part-Object Relationships for Salient Object Detection. In *IEEE ICCV*, 2019.
- [39] Zhiming Luo, Akshaya Mishra, Andrew Achkar, Justin Eichel, Shaozi Li, and Pierre-Marc Jodoin. Non-Local Deep Features for Salient Object Detection. In *IEEE CVPR*, 2017.
- [40] Yuzhen Niu, Yujie Geng, Xueqing Li, and Feng Liu. Leveraging stereopsis for saliency analysis. In *IEEE CVPR*, pages 454–461, 2012.
- [41] Houwen Peng, Bing Li, Weihua Xiong, Weiming Hu, and Rongrong Ji. Rgb-d salient object detection: a benchmark and algorithms. In *ECCV*, pages 92–109, 2014.
- [42] Xuebin Qin, Zichen Zhang, Chenyang Huang, Chao Gao, Masood Dehghan, and Martin Jagersand. BASNet: Boundary-Aware Salient Object Detection. In *IEEE CVPR*, 2019.
- [43] Liangqiong Qu, Shengfeng He, Jiawei Zhang, Jiandong Tian, Yandong Tang, and Qingxiong Yang. RGBD salient object detection via deep fusion. *IEEE TIP*, 26(5):2274–2285, 2017.
- [44] Jianqiang Ren, Xiaojin Gong, Lu Yu, Wenhui Zhou, and Michael Ying Yang. Exploiting Global Priors for RGB-D Saliency Detection. In *IEEE CVPRW*, pages 25–32, 2015.
- [45] Danilo Jimenez Rezende, Shakir Mohamed, and Daan Wierstra. Stochastic Backpropagation and Approximate Inference in Deep Generative Models. In *ICML*, pages 1278–1286, 2014.
- [46] Christian Rupprecht, Iro Laina, Maximilian Baust, Federico Tombari, Gregory D. Hager, and Nassir Navab. Learning in an Uncertain World: Representing Ambiguity Through Multiple Hypotheses. In *IEEE ICCV*, pages 3611–3620, 2017.
- [47] Mohammad Sadegh Aliakbarian, Fatemeh Sadat Saleh, Mathieu Salzmann, Lars Petersson, Stephen Gould, and Amirhossein Habibian. Learning Variations in Human Motion via Mix-and-Match Perturbation. *arXiv e-prints*, page arXiv:1908.00733, 2019.
- [48] Karen Simonyan and Andrew Zisserman. Very Deep Convolutional Networks for Large-Scale Image Recognition. In *ICLR*, 2014.
- [49] Krishna Kumar Singh and Yong Jae Lee. Hide-and-Seek: Forcing a Network to be Meticulous for Weakly-supervised Object and Action Localization. In *IEEE ICCV*, 2017.
- [50] Kihyuk Sohn, Honglak Lee, and Xinchen Yan. Learning Structured Output Representation using Deep Conditional Generative Models. In *NeurIPS*, pages 3483–3491, 2015.
- [51] Hangke Song, Zhi Liu, Huan Du, Guangling Sun, Olivier Le Meur, and Tongwei Ren. Depth-aware salient object detection and segmentation via multiscale discriminative saliency fusion and bootstrap learning. *IEEE TIP*, 26(9):4204–4216, 2017.
- [52] Qingyang Tan, Lin Gao, Yu-Kun Lai, and Shihong Xia. Variational Autoencoders for Deforming 3D Mesh Models. In *IEEE CVPR*, 2018.
- [53] Jacob Walker, Carl Doersch, Harikrishna Mulam, and Martial Hebert. An Uncertain Future: Forecasting from Static Images Using Variational Autoencoders. In *ECCVW*, pages 835–851, 2016.
- [54] Ningning Wang and Xiaojin Gong. Adaptive Fusion for RGB-D Salient Object Detection. *IEEE Access*, 7:55277–55284, 2019.
- [55] Wenguan Wang, Jianbing Shen, Ming-Ming Cheng, and Ling Shao. An Iterative and Cooperative Top-Down and Bottom-Up Inference Network for Salient Object Detection. In *IEEE CVPR*, 2019.
- [56] Yang Wang, Yi Yang, Zhenheng Yang, Liang Zhao, Peng Wang, and Wei Xu. Occlusion Aware Unsupervised Learning of Optical Flow. In *IEEE CVPR*, 2018.
- [57] Rastogi Akash Villegas Ruben Sunkavalli Kalyan Shechman Eli Hadap Sunil Yumer Ersin Lee Honglak Yan, Xinchen. MT-VAE: Learning Motion Transformations to Generate Multimodal Human Dynamics. In *ECCV*, pages 276–293, 2018.
- [58] Maoke Yang, Kun Yu, Chi Zhang, Zhiwei Li, and Kuiyuan Yang. DenseASPP for Semantic Segmentation in Street Scenes. In *IEEE CVPR*, pages 3684–3692, 2018.
- [59] Li Yi, Wang Zhao, He Wang, Minhyuk Sung, and Leonidas J. Guibas. GSPN: Generative Shape Proposal Network for 3D Instance Segmentation in Point Cloud. In *IEEE CVPR*, 2019.
- [60] Shivanthan A. C. Yohanandan, Adrian G. Dyer, Dacheng Tao, and Andy Song. Saliency Preservation in Low-Resolution Grayscale Images. In *ECCV*, 2018.
- [61] Jingjing Li Miao Zhang Huchuan Lu Yongri Piao, Wei Ji. Depth-induced Multi-scale Recurrent Attention Network for Saliency Detection. In *IEEE ICCV*, 2019.
- [62] Jing Zhang, Xin Yu, Aixuan Li, Peipei Song, Bowen Liu, and Yuchao Dai. Weakly-Supervised Salient Object Detection via Scribble Annotations. In *IEEE CVPR*, 2020.
- [63] Jing Zhang, Tong Zhang, Yuchao Dai, Mehrtaash Harandi, and Richard Hartley. Deep Unsupervised Saliency Detection: A Multiple Noisy Labeling Perspective. In *IEEE CVPR*, pages 9029–9038, 2018.
- [64] Jia-Xing Zhao, Yang Cao, Deng-Ping Fan, Ming-Ming Cheng, Xuan-Yi Li, and Le Zhang. Contrast Prior and Fluid Pyramid Integration for RGBD Salient Object Detection. In *IEEE CVPR*, 2019.
- [65] Jia-Xing Zhao, Jiang-Jiang Liu, Deng-Ping Fan, Yang Cao, Jufeng Yang, and Ming-Ming Cheng. EGNet: Edge guidance network for salient object detection. In *IEEE ICCV*, pages 8779–8788, 2019.
- [66] Chunbiao Zhu, Ge Li, Wenmin Wang, and Ronggang Wang. An innovative salient object detection using center-dark channel prior. In *IEEE ICCVW*, 2017.